Available online at www.sciencedirect.com
ScienceDirect
Trans. Nonferrous Met. Soc. China 30(2020) 1816−1825
Transactions of Nonferrous Metals Society of China
www.tnmsc.cn

Effect of rolling reduction and annealing process on microstructure and corrosion behavior of LZ91 alloy sheet

Li-na MA[1], Yan YANG[1,2,3], Gang ZHOU[1], Feng-juan REN[1], Hong-ju DENG[1], Guo-bing WEI[1,3], Xiao-dong Peng[1,3]

1. International Joint Laboratory for Light Alloys,
College of Materials Science and Engineering, Chongqing University, Chongqing 400044, China;
2. State Key Laboratory of Mechanical Transmissions, Chongqing University, Chongqing 400044, China;
3. National Engineering Research Center for Magnesium Alloys, Chongqing University, Chongqing 400044, China

Received 15 December 2019; accepted 26 April 2020

Abstract: The effect of rolling reduction and annealing process on the microstructure and corrosion behavior of Mg−9Li−1Zn (LZ91) alloy was investigated. The test alloy sheets were cold rolled with the reduction of 50% and 75%, respectively, and then were annealed at 200 °C for 1 h. The microstructure of test alloys was observed by OM and SEM while the phase composition was determined by XRD. The corrosion property was evaluated by electrochemical measurements and immersion tests. The results show that LZ91 alloy sheet consists of α-Mg, β-Li and precipitated Mg−Li−Zn compounds ($MgLi_2Zn$ and MgLiZn phases). Dynamic recrystallization grains appear in β-Li phase during annealing process, leading to grain refinement. The results indicate that the increasing rolling reduction and performing the annealing process can enhance the corrosion resistance of LZ91 alloy. The 75% cold-rolled and annealed LZ91 alloy shows the best corrosion resistance.

Key words: LZ91 alloy; cold rolling; annealing; microstructure; corrosion resistance

1 Introduction

Mg−Li alloy as the lightest metallic structural material has attracted increasing attentions in aerospace, weapon and 3C industries due to its high specific strength, excellent forming property and electromagnetic shielding capacity [1−4].

According to the Mg−Li binary phase diagram, when Li content is less than 5.5 wt.%, Mg−Li alloy is composed of single α-Mg phase (hcp), which is Mg solid solution formed by Li dissolved in Mg. When the Li content is between 5.7 and 11 wt.%, the alloy consists of both hcp structured α-Mg and bcc structured β-Li phases. However, when the Li content exceeds 11.5 wt.%, the corresponding alloy is exclusively comprised of the β-Li phase (bcc) [5−7]. Usually, since the α-Mg and β-Li phases are respectively favorable for the improvement of strength and ductility, the α-Mg+ β-Li duplex structured Mg−Li alloy possesses excellent comprehensive mechanical performance, which is one of the most widely used super-light Mg−Li alloys in aerospace and electronics fields. However, the poor corrosion resistance of Mg−Li alloys severely limits their applications. It is well-known that Li as a common reactive metal accelerates the corrosion process of Mg−Li alloy ascribed to its high electrochemical and chemical reactivity [8]. Besides, the porous $Mg(OH)_2$ and

Foundation item: Projects (2016YFB0700403, 2016YFB0301100) supported by the National Key Research and Development Program of China; Project (cstc2019jcyj-msxmX0306) supported by the Chongqing Research Program of Basic Research and Frontier Technology, China; Projects (2018CDGFCL0005, 2018CDJDCL0019) supported by the Fundamental Research Funds for the Central Universities, China; Project (B16007) supported by the 111 Program of Ministry of Education and the State Administration of Foreign Experts Affairs of China

Corresponding author: Yan YANG; Tel: +86-23-65102856; E-mail: yanyang@cqu.edu.cn

DOI: 10.1016/S1003-6326(20)65341-9

Li_2CO_3 films forming on the surface of Mg−Li alloy are not as compact as the passive films like Al_2O_3 in Al alloy [9]. Therefore, there still exists a challenge to find an effective technical means to improve the corrosion resistance of Mg−Li alloy. WANG et al [10] found that the traditional metallurgical process of cold rolling has a significant effect on improving the corrosion resistance of metallic materials through work hardening and protective oxide surface films. LV et al [11] proved that the rolling-induced grain refinement resulted in a better corrosion resistance. Similar results were obtained by NENE et al [12]. In addition, the annealing process is widely performed in industry to eliminate the residual stress and further improve the mechanical property and the microstructure stability of Mg alloy. Meanwhile, the corrosion properties of LZ91 alloy are influenced by the microstructural changes due to annealing process [13,14].

However, there is very limited information on the influence of rolling and annealing processes on the corrosion behavior of Mg−Li alloy, especially the duplex structured Mg−Li alloys. Therefore, the present study is motivated by two objectives. The first is to study the influence of rolling reduction and annealing process on the microstructure of duplex structured LZ91 alloy, while the second is to investigate the effect of rolling reduction and annealing process on the corrosion behavior of LZ91 alloy. The microstructure evolution during the cold rolling and annealing processes is studied with an effort to elucidate the underlying mechanisms governing the corrosion behavior.

2 Experimental

2.1 Alloy preparation

The target alloy is LZ91 alloy ingot with the composition of 9 wt.% Li, 1 wt.% Zn, and balanced Mg. The as-cast LZ91 alloys were machined to 80 mm × 50 mm × 5 mm, and cold rolled with the reduction of 50% and 75%, respectively. Then, the cold-rolled alloy sheets were annealed at 200 °C for 1 h. The samples prepared in this study were denoted in Table 1.

Table 1 Description of sample in experiment

Alloy No.	State
1	As-cast LZ91 alloy sheet
2	50% cold-rolled LZ91 alloy sheet
3	50% cold-rolled and annealed LZ91 alloy sheet
4	75% cold-rolled LZ91 alloy sheet
5	75% cold-rolled and annealed LZ91 alloy sheet

2.2 Microstructural characterization

The microstructure and the corrosion morphology of LZ91 alloy sheets were observed by an optical microscope (OM, Olympus) and a scanning electron microscope (SEM, JEOL JSM 6460LV). The phase composition was analyzed by an X-ray diffractometer (XRD, D/MAX-A) and an X-ray energy dispersive spectrometer (EDS, Genesis 7000).

2.3 Corrosion evaluation

The corrosion properties of LZ91 alloy sheet were analyzed by the electrochemical measurements and immersion tests (i.e. hydrogen evolution and mass loss measurement). The exposed area of samples was on the transverse plane. The samples used for the corrosion tests were cut from the center of the LZ91 alloy sheet with the dimensions of 10 mm × 10 mm. Prior to corrosion tests, the LZ91 samples were wet-ground with $1500^{\#}$ sandpaper to avoid the influence of surface roughness on the corrosion response. The samples were cleaned with alcohol solution and dried by a drying apparatus and then immersed into 3.5 wt.% NaCl solution at room temperature with the exposed surface area of 1 cm^2 (1 cm × 1 cm) for all following corrosion tests.

Electrochemical measurements were performed on a GAMRY electrochemical workstation using the typical three-electrode technique which contains a saturated calomel electrode (SCE) as the reference electrode, Pt as counter electrode and testing material as working electrode. Electrochemical impedance spectroscopy (EIS) tests were performed at open circuit potential, of which the frequency ranged from 1×10^{-2} to 1×10^{4} Hz with a 5 mV amplitude of RMS voltage. The equivalent electrical circuit parameters were obtained from the impedance data processed by the ZView software.

Potentiodynamic polarization curves were recorded with a scan rate of 0.5 mV/s after the stabilization at open circuit potential (OCP). The corrosion density (J_{corr}) and the corrosion

potential (φ_{corr}) of samples were estimated by Tafel fitting [15].

Immersion tests contain hydrogen evolution and mass loss measurement. Corrosion rates of the samples were evaluated by hydrogen evolution, whereas samples were immersed into 3.5 wt.% NaCl solution for 7 days in mass loss measurement. Corrosion products forming on the surface of samples were removed by a cleaning solution (chromic acid) of 25 wt.% CrO_3 at 30 °C thermostatic water bath for 5 min.

All the electrochemical tests and immersion tests were carried out 3 times and the average values were calculated as a result of each test to ensure the accuracy of the experiments.

3 Results

3.1 Microstructure

The XRD patterns of the samples are given in Fig. 1, which reveal that the LZ91 alloy mainly consists of α-Mg phase, β-Li phase and precipitated Mg−Li−Zn compound ($MgLi_2Zn$ and MgLiZn phases). Figure 2 displays the optical microstructures of transverse plane of as-cast LZ91 alloy (Sample 1). It is evidently found from Fig. 2 that the LZ91 alloy exhibits a typical dual-phase structure with some fine black particles. The bright and dark areas are recognized as α-Mg and β-Li phases, respectively. The coarse grains of α-Mg phase and fine black particles distribute disorderly. CHIU et al [16] demonstrated that the ultrafine dispersed particles in the as-cast LZ91 alloy are polygonal MgO and round ZnO, and all particles are smaller than 40 nm, which is in consistent with the EDS results of Alloy 1 shown in Fig. 3.

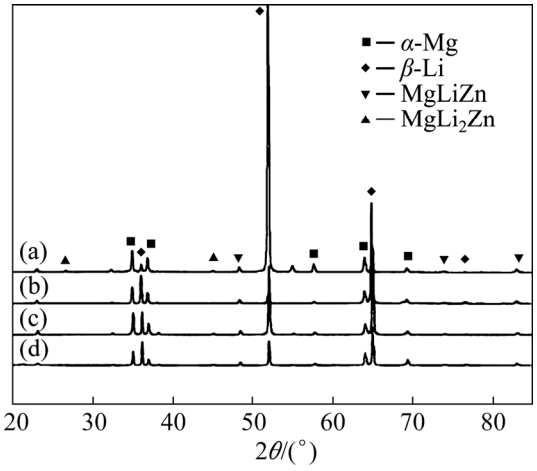

Fig. 1 XRD patterns of LZ91 alloy sheets: (a) Alloy 1; (b) Alloy 2; (c) Alloy 3; (d) Alloy 4; (e) Alloy 5

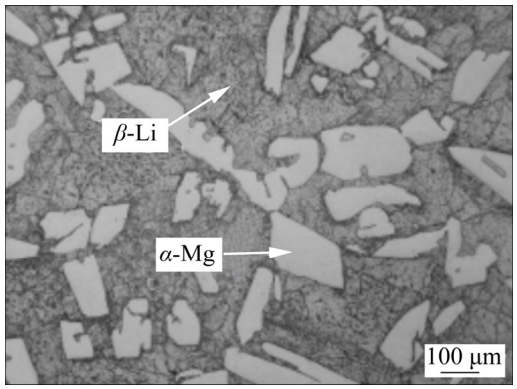

Fig. 2 Optical microstructure of Alloy 1 on transverse plane

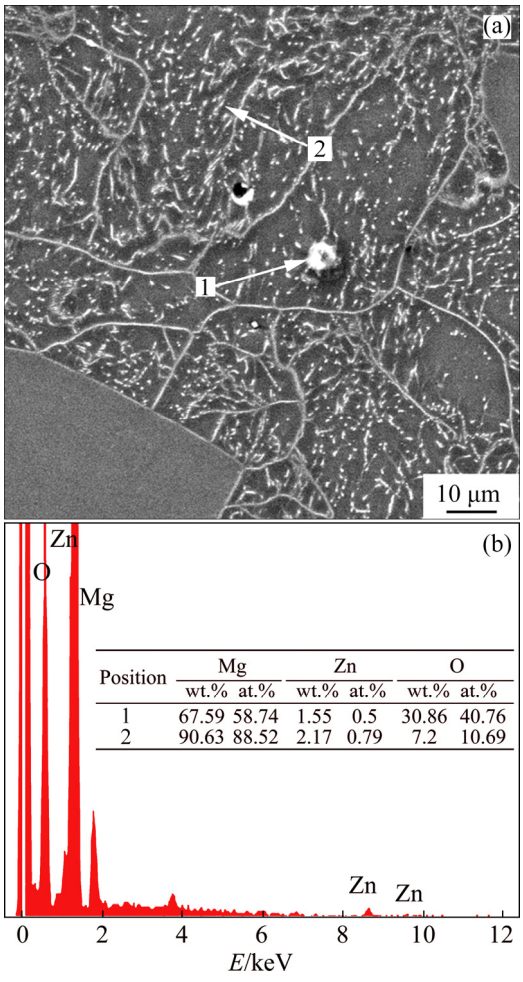

Position	Mg		Zn		O	
	wt.%	at.%	wt.%	at.%	wt.%	at.%
1	67.59	58.74	1.55	0.5	30.86	40.76
2	90.63	88.52	2.17	0.79	7.2	10.69

Fig. 3 SEM image (a) and EDS results (b) of Alloy 1

Figure 4 shows the optical microstructures of transverse planes on Alloys 2−5. The microstructure and phase distribution are changed after cold-rolling and annealing treatments. The as-rolled

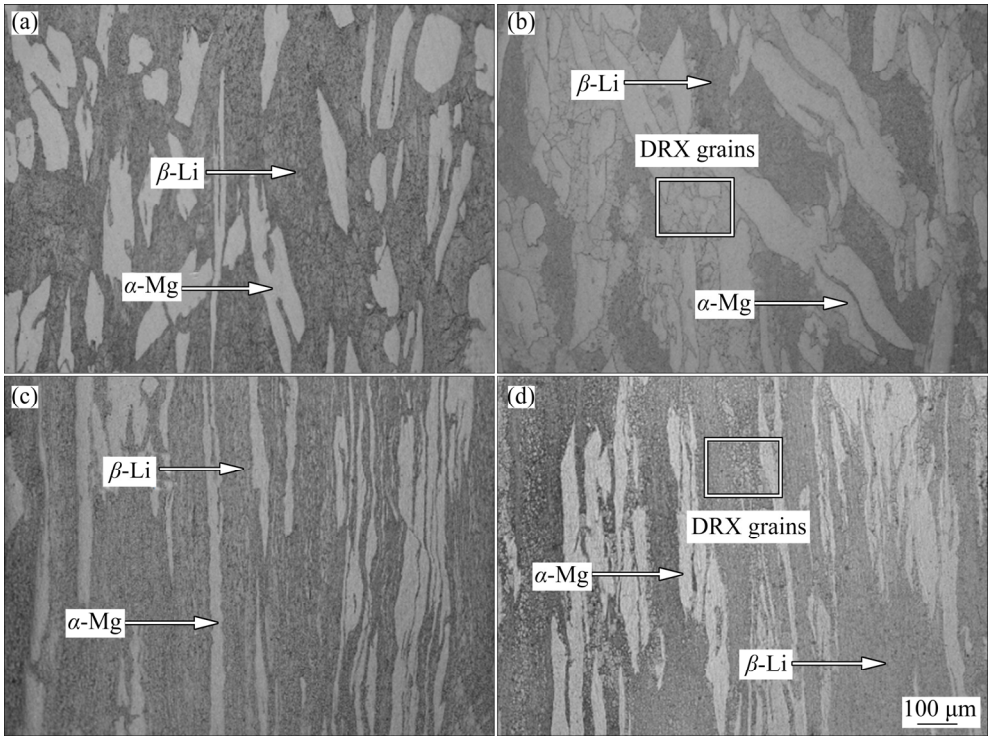

Fig. 4 Optical microstructures of samples on transverse plane: (a) Alloy 2; (b) Alloy 3; (c) Alloy 4; (d) Alloy 5

structure exhibits fibrous rolling texture, which is typical plastically-deformed structure. The α-Mg and β-Li phases are elongated along the rolling direction [17].

When the rolling reduction reaches 75%, the α-Mg phase is aligned distinctly in the rolling direction, as shown in Figs. 4(c, d). The large distortion energy stored in interior of the alloy is induced by cold rolling, which contributes to the increase of the dislocation density and the appearance of dislocation tangles, resulting in the improvement of mechanical properties. Meanwhile, the sufficient deformation energy provided by cold-rolling facilitates the occurrence of dynamic recrystallization (DRX). After annealing process, the microstructure stability is reinforced under the combined effects of distortion energy released and thermal energy. The DRX occurs in LZ91 alloy due to the sufficient driving force at the boundary of α-Mg and β-Li phases. It can be noted from Figs. 4(b, d) that a lot of fine DRX grains forming in the incomplete DRX processes of Alloys 3 and 5 lead to further grain refinement. The increase in the residual stress of alloy after large deformation accelerates the nucleation rate. Moreover, the number of crystal nuclei increases rapidly which partly prevents grain growth and in consequence the grains of Alloy 5 are much smaller than those of Alloy 3.

3.2 Electrochemical properties

3.2.1 Polarization test

Potentiodynamic polarization curves of samples immersed in 3.5 wt.% NaCl solution at room temperature are plotted in Fig. 5 and the values of corrosion potential (φ_{corr}), corrosion current density (J_{corr}) and anodic slope (β_a) are summarized in Table 2. Generally speaking, the values of corrosion potential (φ_{corr}) are close to be

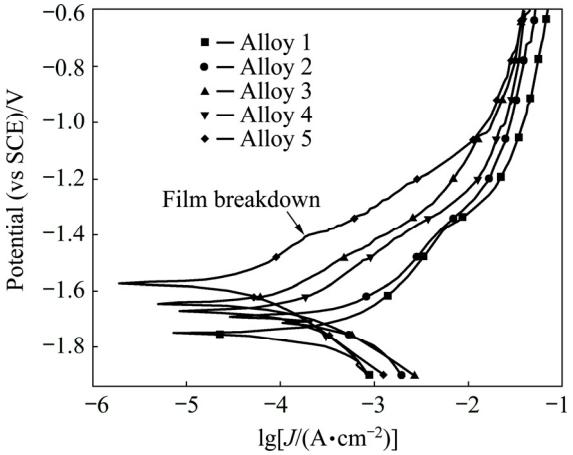

Fig. 5 Potentiodynamic polarization curves of samples immersed in 3.5 wt.% NaCl solution at room temperature

Table 2 Corrosion potential (φ_{corr}), corrosion current density (J_{corr}) and cathodic slope (β_a) of samples obtained from potentiodynamic polarization tests

Alloy No.	φ_{corr} (vs SCE)/ V	J_{corr}/ (A·cm^{-2})	β_a/ (mV·dec^{-1})
1	−1.736±0.02	(56.2±14.5)×10^{-4}	0.196
2	−1.689±0.03	(42.7±7.3)×10^{-4}	0.114
3	−1.668±0.04	(8.7±3.4)×10^{-4}	0.185
4	−1.621±0.02	(8.0±1.2)×10^{-4}	0.205
5	−1.564±0.03	(6.3±0.9)×10^{-4}	0.189

positive with corresponding low values of corrosion current density (J_{corr}) indicating a better corrosion resistances of alloys. By comparing the data in Table 2, the corrosion resistance gets improved with the increase of rolling reduction and after annealing processes. In addition, the corrosion resistance decreases in the order of Alloys 5, 4, 3, 2 and 1. The presence of insoluble protective oxide films ($Mg(OH)_2$/$LiCO_3$) on the alloy surface can be deduced from the obvious existence of passivation region on anodic branch curve of Alloy 5 validated by XU et al [18].

3.2.2 Impedance test

The Nyquist plots of samples obtained from electrochemical impedance spectroscopy (EIS) test are shown in Fig. 6. The impedance diagram clearly exhibits two capacitive loops in all samples. Generally, the capacitive loop in high frequency region is attributed to the relaxation process of electrochemical reaction, while that in low frequency region reflects the presence of surface film and the formation of pitting corrosion affecting the corrosion process [19]. Meanwhile, the radius value of capacitive loop related to the resistance of electrochemical reaction has direct influence on the anodic dissolution rate of alloy. Alloy 5 has the largest radius value of the capacitive loop curve in the Nyquist plots, and it can be concluded explicitly that Alloy 5 presents the best corrosion resistance among the samples. This result is in agreement with that in the polarization test.

The Bode plot and phase angle diagram of samples are shown in Fig. 7. It can be seen that the impedance values of Alloy 5 are much higher than those of other experimental alloys, which is in consistent with the EIS tests, denoting the best corrosion resistance of Alloy 5. Moreover, the Bode plot and phase angle diagram demonstrate two time

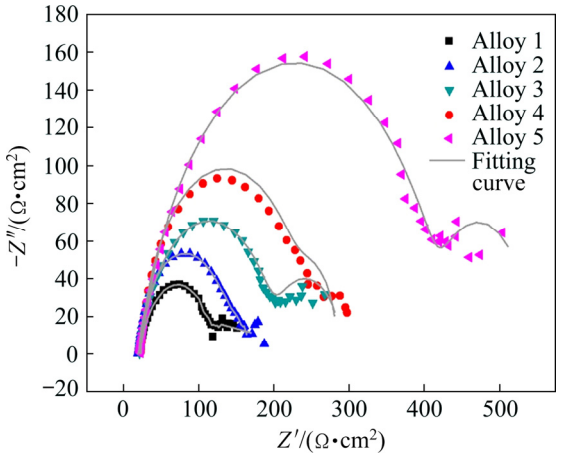

Fig. 6 Nyquist plots of EIS tests of samples performed in 3.5 wt.% NaCl solution at room temperature

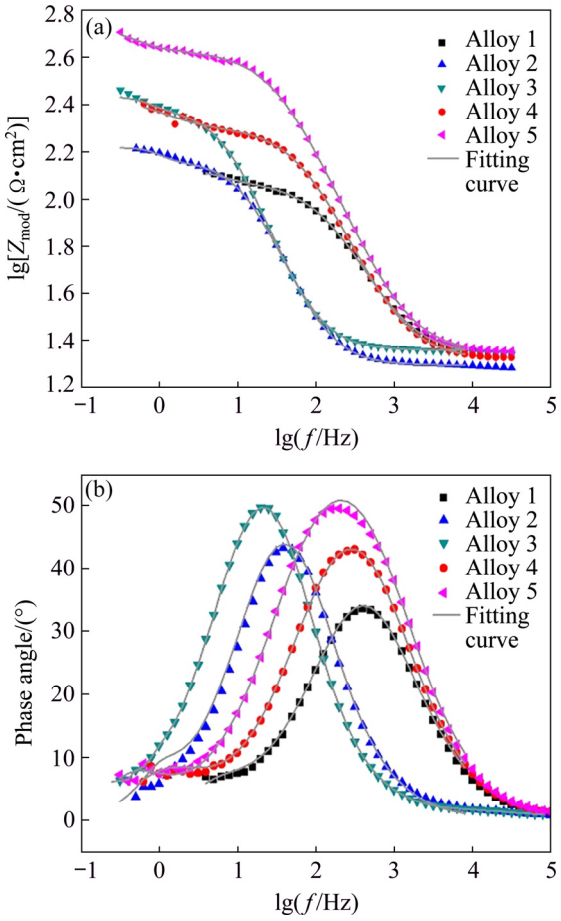

Fig. 7 Impedance plots of samples immersed in 3.5 wt.% NaCl solution at room temperature: (a) Bode plot; (b) Phase angle diagram

constants, because of the double layer capacitance and the corresponding charge transfer resistance during the generation of oxidation films and corrosive products on alloy surface. In general, the above results imply that rolling reduction and

annealing process are the key factors in improving the corrosion resistance of the LZ91 alloy sheet.

To further analyze the corrosion behavior of experimental alloys, the corresponding equivalent circuit and fitting data of the EIS spectra are presented in Fig. 8 and Table 3, respectively. The R_s, R_{ct} and R_f represent solution resistance, charge transfer resistance and film resistance, respectively. WU et al [20] claimed that the higher the R_{ct} and R_f values are, the better the corrosion resistance of alloy presents. The double layer capacity and film capacity are replaced by the constant phase elements (CPE_1 and CPE_2) which are used to compensate the non-homogeneity in the corrosion system. The values of CPE_1 and CPE_2 are related to the corrosion reaction area and the thickness of film forming on the surface, respectively, and higher values indicate larger corrosion area and relatively thinner and more incompact film on the surface of samples [21]. It can be seen in Table 3 that the values of CPE_1 and CPE_2 of experimental alloys rank from high to low as Alloys 1, 2, 3, 4 and 5. The CPE_1 and CPE_2 values of Sample 5 are both the lowest, implying its best corrosion resistance.

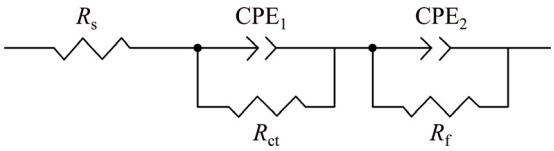

Fig. 8 Equivalent circuits of EIS spectra for all experimental alloys

Table 3 Fitting data of EIS spectra of experimental alloys using equivalent circuits

Alloy No.	R_s/Ω	CPE_1/($10^{-5}\cdot S^n\cdot\Omega^{-1}\cdot cm^{-2}$)	n_1
1	20.27	17.13	0.917
2	19.83	13.93	0.909
3	21.64	9.719	0.825
4	20.62	3.462	0.831
5	21.9	3.005	0.822

Alloy No.	R_{ct}/($\Omega\cdot cm^2$)	CPE_2/($S^n\cdot\Omega^{-1}\cdot cm^{-2}$)	n_2	R_f/($\Omega\cdot cm^2$)
1	124.6	0.0068	1.145	25.24
2	124.8	0.0075	0.957	29.96
3	137.1	0.0063	1.024	47.44
4	181.2	0.0033	0.859	90.87
5	408.3	0.0024	1.058	107.4

Meanwhile, the experimental results prove that the corrosion resistance of sample with larger rolling reduction after annealing is better, which is in agreement with the above results.

3.3 Immersion test

The hydrogen evolution rates of samples as a function of immersion time in 3.5 wt.% NaCl solution are depicted in Fig. 9. The hydrogen evolution rate increases fast at the beginning and then declines gradually, ascribed to protective oxide films and corrosion products forming on alloy surface during corrosion process. A profound difference in hydrogen evolution of samples is discerned with a long immersion time. The descending order of hydrogen evolution rates is Alloys 1, 2, 3, 4 and 5.

Based on mass loss measurements, the corrosion rates of samples after immersion in 3.5 wt.% NaCl solution for 7 days are estimated and given in Fig. 10. It is evidently observed that the corrosion rate of as-cast Alloy 1 is the largest and the corrosion rates of Alloys 4 and 5 are much lower than those of Alloys 2 and 3, attributed to the higher rolling reduction. In addition, the experimental alloys could acquire lower corrosion rate after annealing process corresponding to the result of hydrogen evolution. Thus, it can be proven that large rolling reduction and annealing process play positive roles in improving the corrosion resistance of LZ91 alloy sheet.

4 Discussion

As known, the duplex structured LZ91 alloy has the advantages of low density and excellent plastic formability whereas the poor corrosion resistance severely hinders its applications. In general, corrosion occurs at a rate determined by an equilibrium between opposing electrochemical reactions. The matrix of magnesium alloy as the anode provides enough electrons released and solution species are reduced in cathodic reaction, removing electrons from the metal. The reaction equations of corrosion process are illustrated as follows [22]:

$$Mg \rightarrow Mg^{2+}+2e \quad (1)$$

$$Li \rightarrow Li^{+}+e \quad (2)$$

$$2H_2O+2e \rightarrow H_2\uparrow+2OH^{-} \quad (3)$$

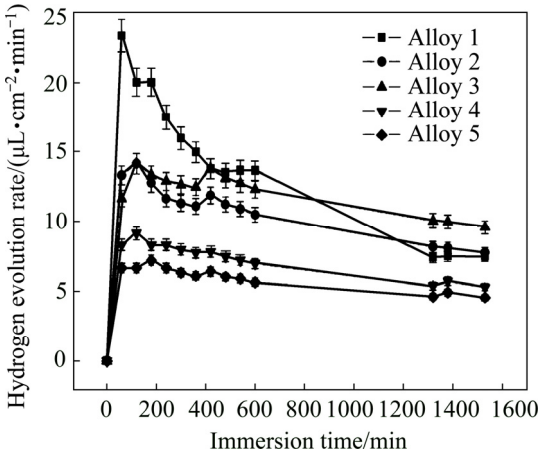

Fig. 9 Plots of hydrogen evolution rates of samples as function of immersion time in 3.5 wt.% NaCl solution at room temperature

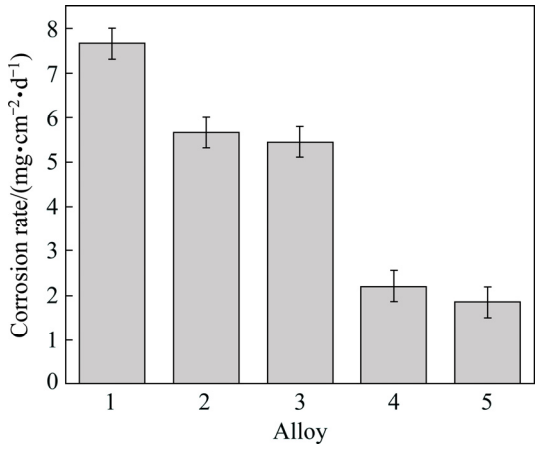

Fig. 10 Mass loss rates of samples after immersion in 3.5 wt.% NaCl solution for 7 d

The surface film contains multiple corrosion products, and the equations of formation process are listed as follows:

$$Mg+2OH^- \rightarrow Mg(OH)_2 \downarrow \quad (4)$$

$$Li+OH^- \rightarrow LiOH \downarrow \quad (5)$$

$$Li_2O+CO_2 \rightarrow Li_2CO_3 \downarrow \quad (6)$$

Such a Li-rich outer layer could react with CO_2 in aqueous environments or the atmosphere to form Li_2CO_3. LI et al [23] claimed that the passivation of LZ91 alloy is facilitated by the compact and protective $LiCO_3$. At the beginning of the corrosion process, the multiple insoluble corrosion products form on the alloy surface as the productive film, and the corresponding alloy would be passivated, preventing the corrosion of NaCl solution. However, the surrounding solution can penetrate continuously through the porous structures of corrosion products and surface films, which results in the breakdown of passive films in local areas, leading to the promotion of chemical reaction with the inner matrix of alloy and the occurrence of significant pitting in a small area.

During the later corrosion process, some parts of the inner alloy are particularly susceptible to corrosion, which depends on the different corrosion potentials of phases. To better indicate the corrosion behavior of LZ91 alloy sheet, the corroded surface morphologies and the illustrations are shown in Fig. 11 and Fig. 12, respectively. It is observed clearly from Fig. 12(a) that the pitting preferentially forming in β-Li phase in the lower electrode potential becomes the spread center. Previous researches [24] claimed that the corrosion reactions took place on two connected dissimilar metals electrically, and the formation of micro-galvanic coupling between different reactivities of α-Mg and β-Li phases would cause the pitting to deepen further in alloys. Figures 12(b, c) show that more pits appear at the phase boundary between α-Mg phase and β-Li phases which expand rapidly and join together with the increase of immersion time due to the difference in corrosion potential. In addition, the number of pits on the surface of β-Li phase is significantly more than that on the α-Mg phase, which proves that pitting mainly extends in the β-Li phase. The adjacent corrosion pits connect with each other to form a larger corrosion area.

The degree of corrosion decreases with the increment of rolling reduction and the process of annealing. Alloy 5 shows the least corrosion pits on alloy surface, suggesting that rolling reduction and annealing process largely improve the corrosion resistance of the LZ91 alloy. SONG et al [25] reported that grain refinement has resulted in the better corrosion resistance attributed to the enhanced passive films forming on the alloy surface. Similar results were certified by XU et al [18] and ACHARYA and SHETTY [26]. According to the experimental results, the grains of experimental alloys get refined with the increase of cold-rolling reduction. The fine grain size creates more grain boundaries providing nucleation sites for the formation of passive films [27], facilitates the formation of a compact oxidation film and the corrosion tends to be uniform as indicated by the

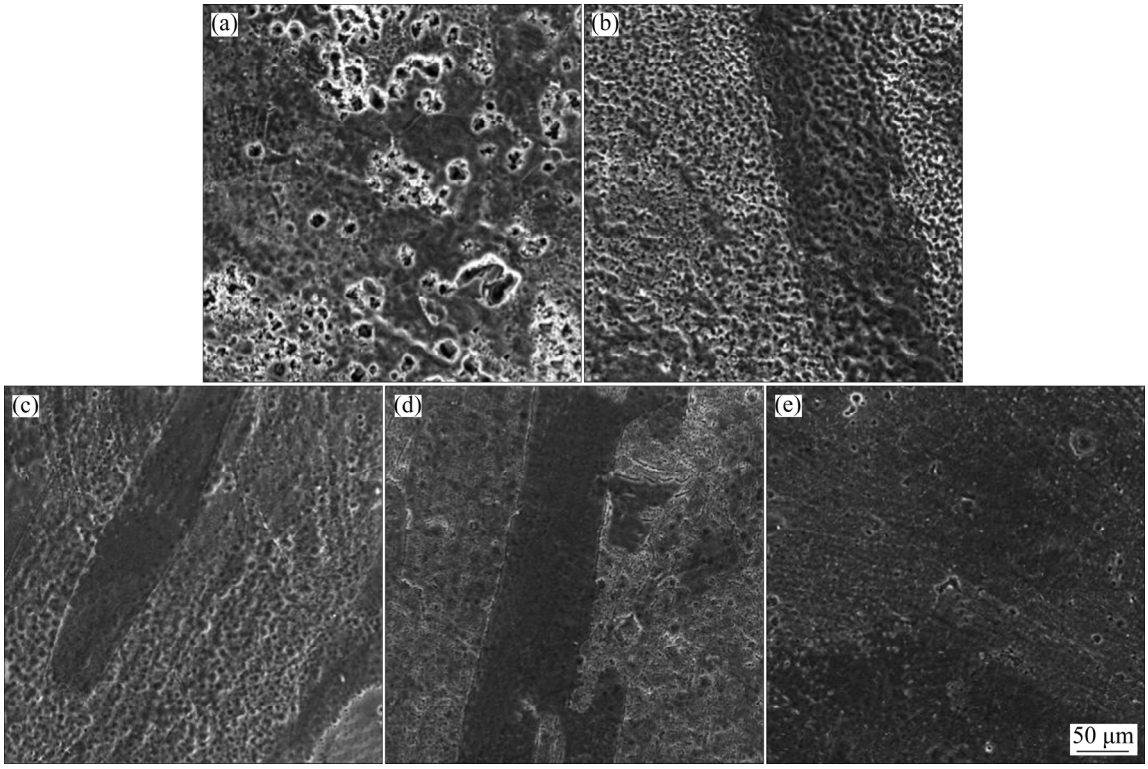

Fig. 11 Corroded surface morphologies of samples after immersion in 3.5 wt.% NaCl solution for 4 h: (a) Alloy 1; (b) Alloy 2; (c) Alloy 3; (d) Alloy 4; (e) Alloy 5

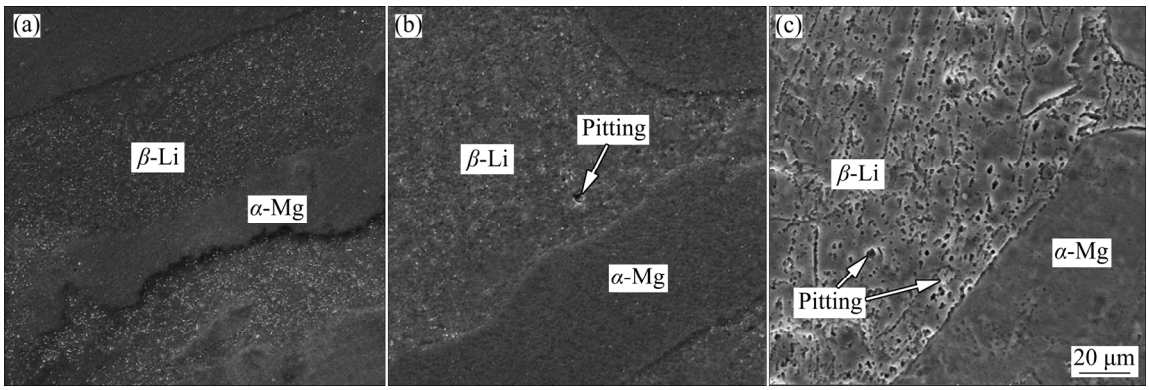

Fig. 12 Illustrations of corrosion process after immersion in 3.5 wt.% NaCl solution for different time: (a) 1 h; (b) 2 h; (c) 4 h

CPE_2 values. Meanwhile, the galvanic couples distribute uniformly after cold rolling treatment, reducing the depth of local corrosion.

The corrosion resistance of cold-rolled alloy is improved after annealing treatment. The high temperature during annealing process causes the decomposition and the occurrence of DRX grains, resulting in the improvement of microstructure stability and further grain refinement. The metastable $MgLi_2Zn$ phase existing in cold-rolled alloy gradually transforms into more stable MgLiZn phase, and the elongated α-Mg phase and stable MgLiZn phase act as physical corrosion barrier restraining the deepening of corrosion. In fact, the rolling reduction and annealing process have critical effects on enhancing the corrosion resistance of LZ91 alloys. The experimental alloys exhibit better corrosion resistances after annealing processes.

5 Conclusions

(1) The LZ91 alloys contain α-Mg, β-Li, $MgLi_2Zn$ and MgLiZn phases. The α-Mg and β-Li

phases are elongated along the rolling direction with increasing the rolling reduction. DRX occurs during annealing process, leading to grain refinement.

(2) The corrosion resistance of LZ91 alloy is enhanced with increasing the rolling reduction and performing the annealing process. The 75% cold-rolled and annealed LZ91 alloy has the best corrosion resistance.

(3) Pitting firstly occurs in the β-Li phase with the lower electrode potential of LZ91 alloy. With the increase of immersion time, more pits appear at the phase boundary between α-Mg phase and β-Li phase which expand rapidly and join together. The number of pits on the surface of β-Li phase is significantly more than that on the α-Mg phase, which proves that pitting mainly extends in the β-Li phase.

References

[1] YANG Yan, PENG Xiao-dong, WEN Hai-ming, ZHENG Bao-long, ZHOU Yi-zhang, XIE Wei-dong, LAVERNIA E J. Influence of extrusion on the microstructure and mechanical behavior of Mg−9Li−3Al−*x*Sr alloys [J]. Metallurgical and Materials Transactions A − Physical Metallurgy and Materials Science, 2013, 44: 1101−1113.

[2] CANDAN S, CANDAN E. Comparative study on corrosion behaviors of Mg−Al−Zn alloys [J]. Transactions of Nonferrous Metals Society of China, 2018, 28: 642−650.

[3] XU Tian-cai, YANG Yan, PENG Xiao-dong, SONG Jiang-feng, PAN Fu-sheng. Overview of advancement and development trend on magnesium alloy [J]. Journal of Magnesium and Alloys, 2019, 7: 536−544.

[4] SUN Yue-hua, WANG Ri-chu, PENG Chao-qun, FENG Yan, YANG Ming. Recent progress in Mg−Li matrix composites [J]. Transactions of Nonferrous Metals Society of China, 2019, 29: 1−14.

[5] DROZD Z, TROJANOVA Z, KUDELA S. Deformation behaviour of Mg−Li−Al alloys [J]. Journal of Alloys and Compounds, 2004, 378: 192−195.

[6] SUN Yue-hua, WANG Ri-chu, PENG Chao-qun, FENG Yan, YANG Ming. Recent progress in Mg−Li matrix composites [J]. Transactions of Nonferrous Metals Society of China, 2019, 29: 1−14.

[7] CHANG Li-li, SHI Chun-chang, CUI Hong-wei. Enhancement of mechanical properties of duplex Mg−9Li−3Al alloy by Sn and Y addition [J]. Transactions of Nonferrous Metals Society of China, 2018, 28: 30−35.

[8] XU Dao-kui, HAN En-hou. Effect of quasicrystalline phase on improving the corrosion resistance of a duplex structured Mg−Li alloy [J]. Scripta Materialia, 2014, 71: 21−24.

[9] XIANG Qing, JIANG Bin, ZHANG Yu-xin, CHEN Xiao-bo, SONG Jiang-feng, XU Jun-yao, FANG Liang, PAN Fu-sheng. Effect of rolling-induced microstructure on corrosion behaviour of an as-extruded Mg−5Li−1Al alloy sheet [J]. Corrosion Science, 2017, 119: 14−22.

[10] WANG Bao-jie, XU Dao-kui, WANG Shi-dong, SHENG Li-yuan, ZENG Rong-chang, HAN En-hou. Influence of solution treatment on the corrosion fatigue behavior of an as-forged Mg−Zn−Y−Zr alloy [J]. International Journal of Fatigue, 2019, 120: 46−55.

[11] LV Jin-long, LUO Hong-yun. The effects of cold rolling temperature on corrosion resistance of pure iron [J]. Applied Surface Science, 2014, 317: 125−130.

[12] NENE S S, KASHYAP B P, PRABHU N, ESTRIN Y, AL-SAMMAN T. Microstructure refinement and its effect on specific strength and bio-corrosion resistance in ultralight Mg−4Li−1Ca (LC41) alloy by hot rolling [J]. Journal of Alloys and Compounds, 2014, 615: 501−506.

[13] LIU Gang, MA Zhen-duo, WEI Guo-bing, XU Tian-cai, ZHANG Xi, YANG Yan, XIE Wei-dong, PENG Xiao-dong. Microstructure, tensile properties and corrosion behavior of friction stir processed Mg−9Li−1Zn alloy [J]. Journal of Materials Processing Technology, 2019, 267: 393−402.

[14] ZHANG Cheng, WU Liang, ZHAO Zi-long, XIE Zhi-hui, HUANG Guang-sheng, LIU Lei, JIANG Bin, ATRENS A, PAN Fu-sheng. Effect of Li content on microstructure and mechanical property of Mg−*x*Li−3(Al−Si) alloys [J]. Transactions of Nonferrous Metals Society of China, 2019, 29: 2506−2513.

[15] CAO Fa-he, CAO Jiang-lin, ZHANG Zhao, Jian-qian, CAO Chu-nan. Plasma electrolytic oxidation of AZ91D magnesium alloy with different additives and its corrosion behavior [J]. Materials and Corrosion − Werkstoffe Und Korrosion, 2007, 58: 676−683.

[16] CHIU Chui-hung, WU Homg-yu, WANG Jiah-yih, LEE Shyong. Microstructure and mechanical behavior of LZ91 Mg alloy processed by rolling and heat treatments [J]. Journal of Alloys and Compounds, 2008, 460: 246−252.

[17] MA Ru, LU Yue, WANG Ling, WANG Yi-nong. Influence of rolling route on microstructure and mechanical properties of AZ31 magnesium alloy during asymmetric reduction rolling [J]. Transactions of Nonferrous Metals Society of China, 2018, 28: 902−911.

[18] XU Wang-qiang, BIRBILIS N, SHA Gang, WANG Yu, DANIELS J E, XIAO Yang, FERRY M. A high-specific-strength and corrosion-resistant magnesium alloy [J]. Nature Materials, 2015, 14: 1229−1235.

[19] LELEU S, RIVES B, CAUSSE N, PEBERE N. Corrosion rate determination of rare-earth Mg alloys in a Na_2SO_4 solution by electrochemical measurements and inductive coupled plasma-optical emission spectroscopy [J]. Journal of Magnesium and Alloys, 2019, 7: 47−57.

[20] WU Peng-peng, XU Fang-jun, DENG Kun-kun, HAN Fu-yin, ZHANG Zhong-zhong, GAO Rui. Effect of extrusion on corrosion properties of Mg−2Ca−*x*Al (*x*=0, 2, 3, 5) alloys [J]. Corrosion Science, 2017, 127: 280−290.

[21] LI Jia-run, JIANG Quan-tong, SUN Hu-yuan, LI Yan-tao. Effect of heat treatment on corrosion behavior of AZ63 magnesium alloy in 3.5 wt.% sodium chloride solution [J]. Corrosion Science, 2016, 111: 288−301.

[22] LIU Gang, XIE Wen, WEI Guo-bing, YANG Yan, LIU Jun-wei, XU Tian-cai, XIE Wei-dong, PENG Xiao-dong. Dynamic recrystallization behavior and corrosion resistance of a dual-phase Mg−Li alloy [J]. Materials, 2018, 11(3): 1−11.

[23] LI Chuan-qiang, XU Dao-kui, CHEN Xiao-bo, WANG Bao-jie, WU Rui-zhi, HAN En-hou, BIRBILIS N. Composition and microstructure dependent corrosion behaviour of Mg−Li alloys [J]. Electrochimica Acta, 2018, 260: 55−64.

[24] CHOWDARY S V, DUMPALA R, KUMAR A S, KONDAIAH V V, SUNIL R B. Influence of heat treatment on the machinability and corrosion behavior of AZ91 Mg alloy [J]. Journal of Magnesium and Alloys, 2018, 6: 52−58.

[25] SONG Guang-ling, ATRENS A, DARGUSCH M. Influence of microstructure on the corrosion of diecast AZ91D [J]. Corrosion Science, 1999, 41: 249−273.

[26] ACHARYA M G, SHETTY A N. The corrosion behavior of AZ31 alloy in chloride and sulfate media − A comparative study through electrochemical investigations [J]. Journal of Magnesium and Alloys, 2019, 7: 98−112.

[27] AUNG N N, ZHOU Wei. Effect of grain size and twins on corrosion behaviour of AZ31B magnesium alloy [J]. Corrosion Science, 2010, 52: 589−594.

轧制变形量及轧后退火对 LZ91 镁合金板材显微组织和耐腐蚀性能的影响

马丽娜[1]，杨 艳[1,2,3]，周 港[1]，任凤娟[1]，邓洪举[1]，魏国兵[1,3]，彭晓东[1,3]

1. 重庆大学 材料科学与工程学院 轻合金材料国际合作联合实验室，重庆 400044；
2. 重庆大学 机械传动国家实验室，重庆 400044；
3. 重庆大学 国家镁合金材料工程技术研究中心，重庆 400044

摘 要：研究轧制变形量和轧后退火工艺对 Mg−9Li−1Zn (LZ91) 合金显微组织和耐腐蚀性能的影响。采用冷轧变形工艺制备轧制压下量分别为 50%和 75%的 LZ91 镁合金板材，然后在 200 ℃ 下退火 1 h。采用光学显微镜和扫描电子显微镜观察合金的显微组织，用 X 射线衍射仪测定合金中的相组成。结果表明，LZ91 镁合金由 α-Mg、β-Li 和 Mg−Li−Zn 三元化合物($MgLi_2Zn$ 和 MgLiZn 相)组成。退火过程中 β-Li 相发生动态再结晶，合金晶粒细化。腐蚀试验表明：轧制变形和轧后退火能显著改善 LZ91 合金的耐腐蚀性能，75%冷轧退火 LZ91 镁合金具有最好的耐蚀性。

关键词：LZ91 镁合金；冷轧；退火；显微组织；耐腐蚀性

(Edited by Bing YANG)